Supporting Information:

Antagonistic Role of Aqueous Complexation in the Solvent Extraction and Separation of Rare Earth Ions

Pan Sun[1], Erik A. Binter[2], Zhu Liang[2†], M. Alex Brown[3], Artem V. Gelis[4], Ilan Benjamin[5], Mrinal K. Bera[1], Binhua Lin[1], Wei Bu[1]*, Mark L. Schlossman[2]*

[1]NSF's ChemMatCARS, Pritzker School of Molecular Engineering, University of Chicago, Chicago, IL 60637, USA.

[2]Department of Physics, University of Illinois at Chicago, Chicago, IL 60607, USA.

[3]Chemical and Fuel Cycle Technologies Division, Argonne National Laboratory, Lemont, IL, 60439, USA.

[4]Radiochemistry Program, Department of Chemistry and Biochemistry, University of Nevada, Las Vegas, NV, 89141, USA.

[5]Department of Chemistry and Biochemistry, University of California, Santa Cruz, California 95064, USA

[°]E-mail: schloss@uic.edu, bu@cars.uchicago.edu.

Safety Statement. No unexpected or unusually high safety hazards were encountered in any aspect of this work.

1. Experimental Details

All measurements were taken at a room temperature of 22°C.

1.1. Materials. Ultrapure water from a Millipore system with resistivity of 18.2 MΩ•cm was used for all aqueous solutions. Bis(2-ethylhexyl)-phosphoric acid (HDEHP, after purification, >99.9%, Chart 1) was purchased from Alfa-Aesar (97%) and purified via a third-phase formation procedure.[1] $NdCl_3 \cdot 6H_2O$ (99.9%), $ErCl_3 \cdot 6H_2O$ (99.995%), $LuCl_3 \cdot 6H_2O$ (99.99%), $GdCl_3 \cdot 6H_2O$ (99.99%), and $DyCl_3 \cdot 6H_2O$ (99.9%), were purchased from Sigma Aldrich and used without further purification. $LaCl_3 \cdot 7H_2O$ (99.99%) was purchased from Alfa-Aesar and used without further purification. Dihexadecyl phosphoric acid (DHDP, >98% purity from Sigma-Aldrich, Chart 1) was purified by recrystallizing it twice from chloroform. Sodium hydroxide (NaOH) was purchased from Alfa-Aesar (98%). Hydrogen chloride (HCl) was purchased from Fisher Chemical (36.5 to 38.0%).

1.2. Preparation of saturated HDEHP aqueous solution. Aqueous solutions of HDEHP and lanthanide chlorides ($LnCl_3$) were prepared at three different values of pH: 2.0, 3.0, and 4.5. Saturated HDEHP aqueous solution was prepared by adding 2 g HDEHP into 2 L water and mixing for 30 minutes by shaking by hand. The solution was then allowed to phase separate for at least 24 hours. Then, the solution was filtered through Omnipore filter paper (pore size of 0.2 μm) to obtain a clear solution. The concentration of HDEHP in the saturated HDEHP solution was measured to be close to 300 μM (at pH 3.4) by ICP-OES. HDEHP solutions used in the experiments were made by diluting the saturated HDEHP aqueous solution by a factor of 30 with pure water to yield a concentration of 10±1 μM, as measured by ICP-OES. Then, a certain volume of lanthanide salt aqueous solution (concentration of 1mM) was added into the diluted HDEHP aqueous solution (the ratio of HDEHP to lanthanides is 6:1). After that, the pH was adjusted with NaOH or HCl.

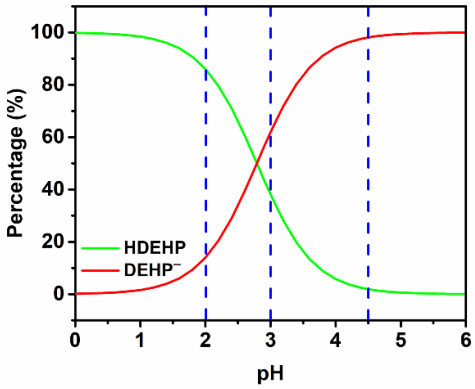

Figure S1. The ratio of HDEHP and $DEHP^-$ in aqueous solution as a function of pH. The blue dashed lines represent experimental conditions in the present study. The pK_a value of HDEHP is 3.24 according to previous literature.[2]

Figure S1 shows the percentage of HDEHP and $DEHP^-$ in aqueous solution as a function of pH. HDEHP will deprotonate to $DEHP^-$ as the pH increases. In the present study, we select three pH values to control the existing form of extractant in the aqueous solution: 5% $DEHP^-$ and 95% HDEHP at pH 2.0, 37% $DEHP^-$ and 63% HDEHP at

pH 3.0, and 95% $DEHP^-$ and 5% HDEHP at pH 4.5. Note that the presence of lanthanides can change these percentages as the protron and the Ln(III) compete for $DEHP^-$.

1.3. Surface Tension Measurements. The tension of HDEHP-solutions was measured with the Wilhelmy plate method using a KSV NIMA tensiometry balance with a filter paper (Whatman Chr 1 with the width of 1 cm). The experimental HDEHP aqueous solution was poured into the trough, then the Wilhelmy plate (pre-equilibrated with pure water) was lowered to touch the surface of the aqueous solution, this point was defined to be $t = 0$ in our time-dependent tension measurement (Fig. 2A, B, and C). Table S1 shows the equilibrium value of surface tension for different lanthanides at different pH (Fig. 2D). Both X-ray reflectivity and XFNTR measurement are taken after the surface tension has reached its equilibrium value. Note that samples containing HDEHP-Er at pH 4.5 were made about 17 hours before the X-ray reflectivity and XFNTR measurements to ensure sample equilibration.

Table S1. The equilibrium value of surface tension shown in Fig. 2 for different lanthanides at different pH

Components	pH 2.0	pH 3.0	pH 4.5
no Ln ions	43.8 mN/m	54.1	66.5
La	43.2	49.8	52.4
Nd	45.6	53.7	56 .2
Gd	50.5	56.8	60.9
Dy	51.1	59.3	64.8
Er	51.0	59.6	66.6
Lu	51.7	60.0	67.8

The experimental uncertainty of surface tension values are ±0.2 mN/m.

Figure S2 shows the surface tension curves for single-Ln HDEHP aqueous solutions, which are the same curves as in Fig. 2 of the main paper, plus curves for mixtures of Er and Nd which are labeled Er+Nd. The ratio of HDEHP to each Ln is 6:1, indicating that the ionic strength of the mixture is twice that of single-Ln solutions.

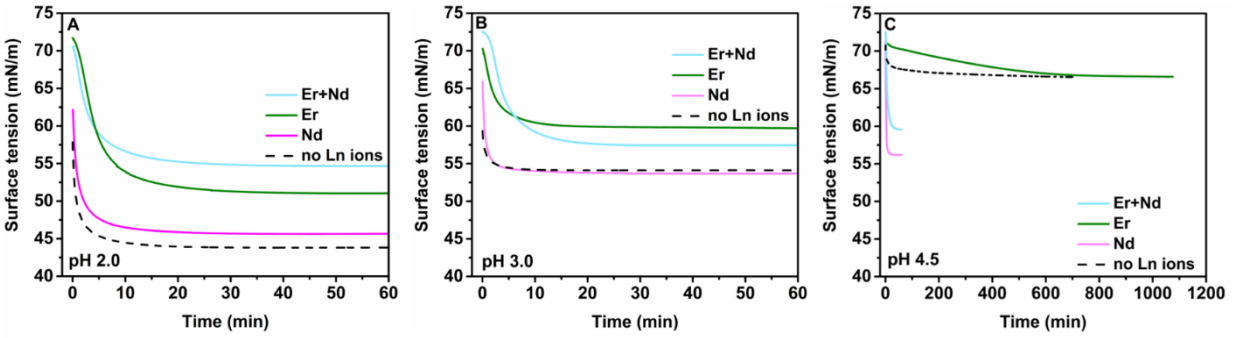

Figure S2. Time dependent surface tension of HDEHP aqueous solutions containing different lanthanide ions at various pH. (A) pH 2.0, (B) pH 3.0, (C) pH 4.5.

To measure the critical aggregation concentration (CAC) of HDHEP in the aqueous solution, the surface tension of aqueous solutions containing different concentration of HDEHP were measured. The pH of all HDEHP-aqueous solutions was adjusted to 1.6 to ensure that most of the HDEHP was protonated. The result is shown in Figure S3.

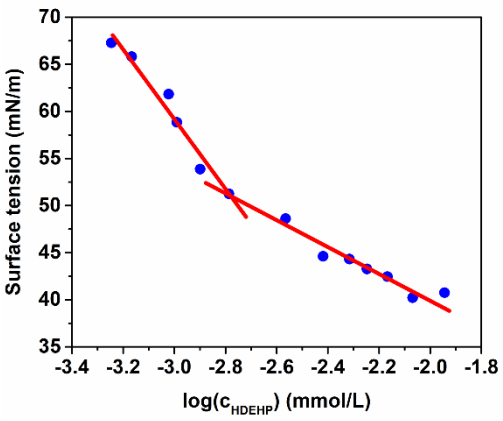

Figure S3. Surface tension of HDEHP-aqueous solution as a function of the concentration of HDEHP at pH 1.6. The CAC is determined to be around 1.6 μM by the intersection of the two red lines.

1.4. X-ray Instrumentation and Langmuir Trough Setup. Synchrotron X-ray experiments were conducted with a liquid surface scattering instrument located at beamline 15-ID, NSF's ChemMatCARS, of the Advanced Photon Source, Argonne National Laboratory.[3] X-ray energy was set to 10 keV. The Langmuir trough was inside a closed box, which was purged with helium to reduce the beam damage and the air scattering.[4] The helium was bubbled through water prior to entering the trough box. Beam damage was avoided by collecting data in appropriate time intervals as indicated by previous tests. The sample was shifted horizontally to place the x-ray beam on a fresh spot on the sample between scans.

1.5. X-ray Reflectivity. Reflectivity data were measured as a function of wave vector transfer, $Q_z = \left|\vec{k_s} - \vec{k_i}\right| = 2k_0 \sin\alpha$, where $k_0 = 2\pi/\lambda$ is the wavenumber, $\vec{k_i}$ is the incident wave vector, and $\vec{k_s}$ is the scattered or reflected wave vector. The reflectivity data at each Q_z consists of the measurement of the specularly reflected X-ray intensity (at $Q_{xy} = 0$) and the background intensity measured slightly off from the specular condition (i.e., $Q_{xy} \neq 0$ but small), which are done simultaneously by using Pilatus 200K area detector. Both intensities are normalized to the incident beam intensity prior to further analysis. The slits prior to the sample set the beam size incident on the sample and had an opening of 60 μm × 2 mm (vertical by horizontal) at low Q_z and 100 μm × 2 mm at high Q_z. The length of the footprint of the X-ray beam on the water surface varied from 1.3 mm to 40 mm as the incident angle decreased.

X-ray reflectivity data were measured on equilibrated samples. This involved first waiting for the equilibration of the surface tension. Then multiple reflectivity measurements were taken over short ranges in Q_z to check for stability. Only after both the surface tension and the x-ray reflectivity values were stable was the full measurement made. In some cases, the sample was prepared well ahead of time to ensure that it was in equilibrium when the beam was available. For example, samples containing HDEHP-Er at pH 4.5 were prepared about 17 hours before the X-ray reflectivity measurement to ensure sample equilibration.

X-ray reflectivity data were fit to a model functional form to determine the electron density profile $\rho(z)$ along the direction z perpendicular to the interface, but averaged over the x–y plane of the interface. The model is a sum of error functions:

$$\rho(z) = \frac{1}{2}\sum_{i=0}^{N} \mathrm{erf}\left(\frac{z-z_i}{\sqrt{2}\sigma}\right)(\rho_i - \rho_{i+1}) + \frac{\rho_0+\rho_{N+1}}{2}, \quad (1)$$

where $\mathrm{erf}(z) = (2/\sqrt{\pi})\int_0^z e^{-t^2}dt$; N is the number of slabs; ρ_i is the electron density of the ith slab where $\rho_0 = \rho_{\mathrm{water}}$ and $\rho_{N+1} = \rho_{\mathrm{air}}$ are, respectively, the electron densities of the bulk water and air phases; z_i is the position of the ith interface; and σ is the interfacial roughness. The thickness of the ith slab, d_i, is defined as $|z_i - z_{i-1}|$. X-ray reflectivity is calculated using the Parratt formalism by discretizing the density profile in Eq. 1. Additional fitting parameters include Q_z offset to correct for small misalignments of the instrument and a scale factor.

Figure S4 illustrates the zero-roughness electron density profiles that correspond to the electron density profiles shown in Figure 3 to reveal the underlying layer structure in the absence of capillary wave roughening.

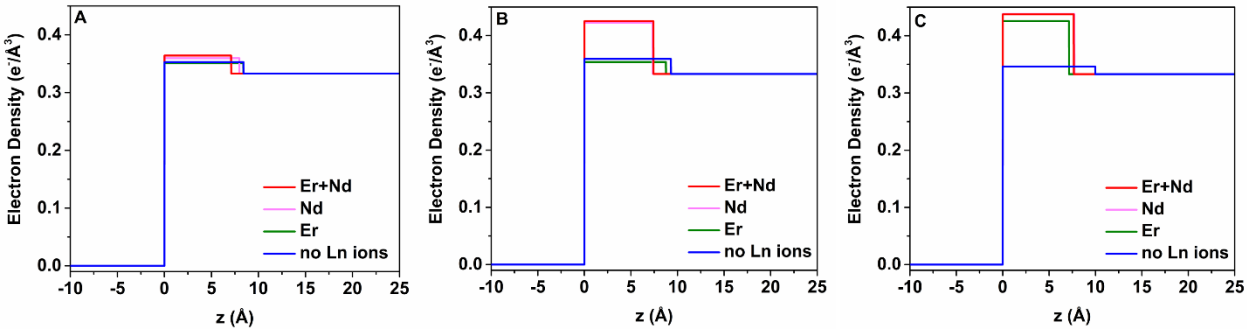

Figure S4. Electron density profiles as a function of the distance z normal to the liquid-vapor interface in the absence of capillary wave roughening. (A: pH 2.0, B: pH 3.0, C: pH 4.5)

1.6. X-ray Fluorescence Near Total Reflection (XFNTR). XFNTR data consists of measurements of fluorescence spectra from samples for a series of Q_z near the critical Q_c for total reflection. A Vortex-60EX multi-cathode energy dispersive X-ray detector, placed perpendicularly above the surface, recorded the X-ray fluorescence spectrum. The fluorescence spectrum was then normalized to the incident beam intensity and corrected for detector dead time. After normalization, the Lα1 fluorescence peak of lanthanide (Nd: 5255 eV; Er: 6970 eV) was fit to a Gaussian function to get its integrated area, which provides the XFNTR signal. The XFNTR signal is modeled by integrating the X-ray intensity and the lanthanide ion concentration over the overlap region between the detection volume and the X-ray path in the aqueous phase. The details have been described in our previous work.[5-6]

XFNTR data were measured on equilibrated samples, unless stated otherwise. This involved first waiting for the equilibration of the surface tension. For most samples, x-ray reflectivity was measured next, as described above. Then multiple XFNTR measurements were taken over short ranges in Q_z to check for stability. Only after both the surface tension and XFNTR values were stable was the full measurement made. In some cases, the sample was prepared well ahead of time to ensure that it was in equilibrium when the beam was available. For example, samples

containing HDEHP-Er at pH 4.5 were prepared about 17 hours before the XFNTR measurement to ensure sample equilibration.

Figure S5A illustrates the fluorescence spectrum of Er and Nd from reference samples. The $L\alpha_1$ fluorescence peak of Nd is far from the $L\alpha_1$ peak of Er, which means that we can distinguish Er and Nd in our fluorescence spectra from mixture samples. However, Nd has a weak $L\gamma_3$ peak, which overlaps the $L\alpha_1$ peak of Er. For the case of pH 2.0, the signal of Nd-$L\alpha_1$ and Er-$L\alpha_1$ were close, as shown in Figure S5B. The analysis of the Er peak in this and similar cases was performed by subtracting the Nd-$L\gamma_3$ peak from the Er-$L\alpha_1$ peak. For the case of pH 3.0, it was found that the intensity of peaks in the region between 6250 and 7500 eV were almost the same between samples containing only Nd and samples containing a mixture of Er and Nd (Figure S5C). A similar result was also found in the case of pH 4.5 (Figure S5D).

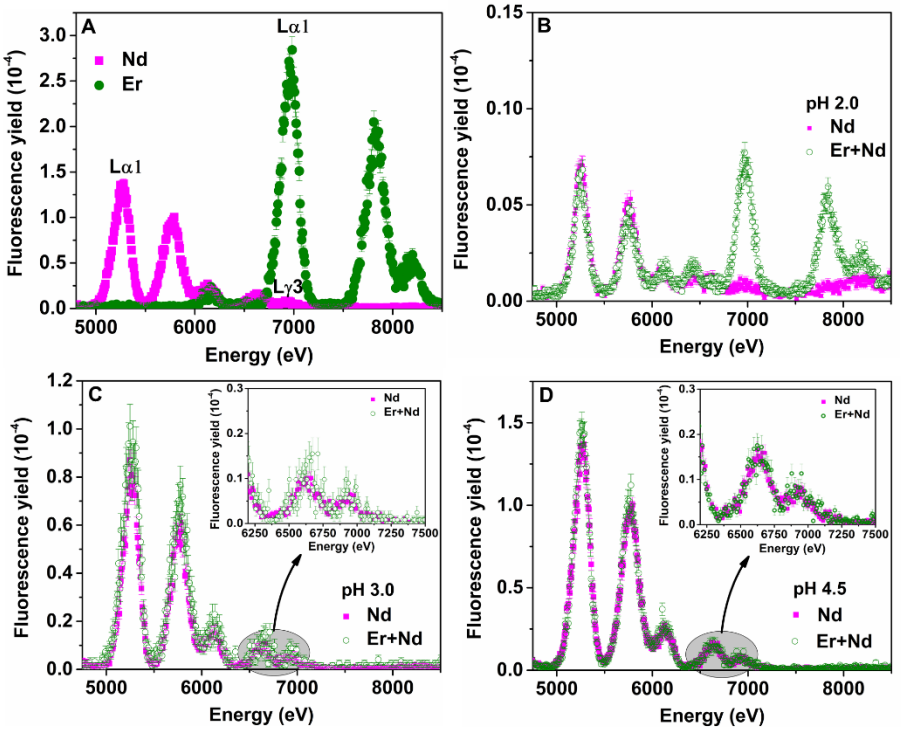

Figure S5. (A) Normalized fluorescence spectra from the reference samples containing either Nd or Er at Q_z = 0.015 Å^{-1}. Normalized fluorescence spectra from samples containing Nd and a mixture of Nd and Er at Q_z = 0.015 Å^{-1} for pH 2.0 (B), 3.0 (C) and 4.5 (D).

To obtain the interfacial coverage of lanthanide ions on the water surface, the scale factor determined by the scattering geometry and elements needs to be obtained from the reference sample containing specific lanthanide ions.[5] Here, XFNTR were measured from 50 mM $NdCl_3$ and $ErCl_3$ solutions, respectively. As shown in Figure S6, the X-ray fluorescence yield of Er is higher than that of Nd. The scale factors for Nd and Er are 1.32×10^{-8} ($\pm 3.4 \times 10^{-10}$) Å and 3.57×10^{-8} ($\pm 7.1 \times 10^{-10}$) Å, respectively.

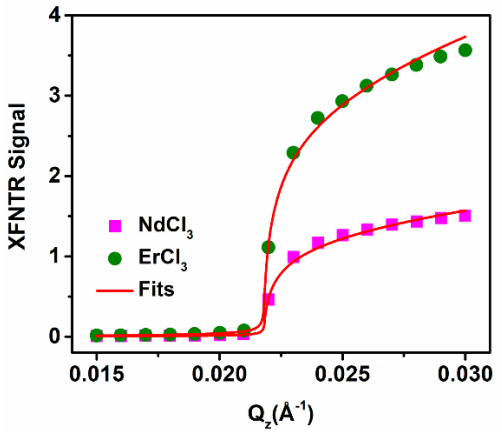

Figure S6. The integrated fluorescence intensities of Nd and Er Lα$_1$ emission line from reference samples (concentration of Nd and Er are both 50 mM) are shown as a function of wave vector transfer Q_z. The solid lines are the best fits that determine the scale factor of 1.32×10^{-8} ($\pm 3.4 \times 10^{-10}$) Å (Nd) and 3.57×10^{-8} ($\pm 7.1 \times 10^{-10}$) Å (Er).

Table S2. Interfacial density of Nd and Er in Figures 4C and 4D.

	Single-component Ln ion solutions		Mixture of Er and Nd ion solutions	
pH	Interfacial density of Nd (number of ions per Å^2)	Interfacial density of Er (number of ions per Å^2)	Interfacial density of Nd (number of ions per Å^2)	Interfacial density of Er (number of ions per Å^2)
2.0	2.13×10^{-4} ($\pm8\times10^{-6}$)	5.0×10^{-5} ($\pm5\times10^{-6}$)	1.90×10^{-4} ($\pm8\times10^{-6}$)	6×10^{-5} ($\pm1\times10^{-5}$)
3.0	2.5×10^{-3} ($\pm1\times10^{-4}$)	1.53×10^{-4} ($\pm6\times10^{-6}$)	2.8×10^{-3} ($\pm1\times10^{-4}$)	BDL
4.5	4.2×10^{-3} ($\pm2\times10^{-4}$)	3.19×10^{-3} ($\pm7\times10^{-5}$)	4.2×10^{-3} ($\pm2\times10^{-4}$)	BDL

BDL – below detection limit (<2 x 10^{-5})

The adsorption of Er-(H)DEHP complex on the water surface can be an extremely slow process as indicated by the kinetics of surface tension result. Here, we measured the time dependence of XFNTR data for HDEHP-aqueous solution containing Er with pH 4.5, as shown in Figure S7. The interfacial coverage of Er increased slowly within the first 2 hours and increased by a factor of 3.2 after 17 hours when the surface tension reached the equilibration value.

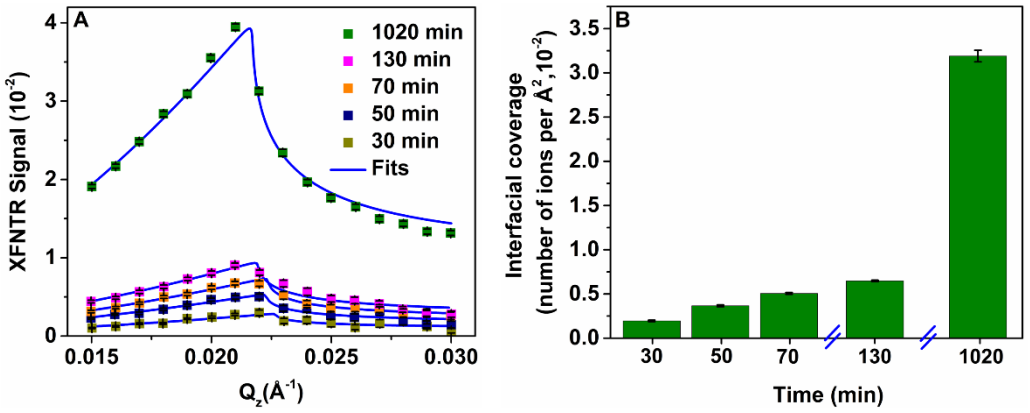

Figure S7. (A) X-ray fluorescence near total reflection (XFNTR) as a function of the wave vector transfer Q_z near the critical $Q_c \approx 0.217$ Å^{-1} for total reflection at different time. Measurements were from samples containing single ionic components, Er at pH 4.5. (B) Interfacial density of ions (number per area) as a function of time.

1.7. X-ray Fluorescence Near Total Reflection (XFNTR) measurement of adsorption of Er and Nd to DHDP monolayers.

Monolayers of DHDP were prepared by spreading DHDP-chloroform solution (1 mg/mL) on the surface of aqueous solutions containing a 1:1 mixture of $NdCl_3$ and $ErCl_3$ (concentration of each salt was 10 μM, aqueous pH was 2.5). The surface pressure of DHDP monolayer was controlled at 10 mN/m by a Teflon barrier. XFNTR of DHDP monolayers were measured at different times as shown in the Figure S6. The interfacial coverage obtained from the fitting of XFNTR data is presented in Table S3.

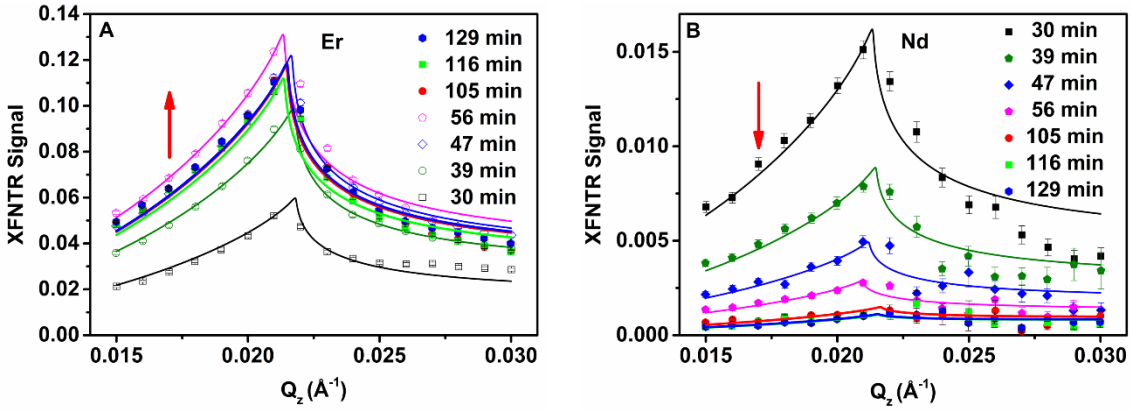

Figure S8. Time dependence of X-ray fluorescence near total reflection (XFNTR) as a function of wave vector transfer Q_z near the critical $Q_c \approx 0.217$ Å^{-1} for total reflection from the DHDP monolayer on a solution containing a 1:1 mixture of $NdCl_3$ and $ErCl_3$.

Table S3. Interfacial density of Er and Nd in Figures 7 and S8.

Time (min)	Er (number of ions per Å^2)	Nd (number of ions per Å^2)
30	4.3×10^{-3} ($\pm2\times10^{-4}$)	3.1×10^{-3} ($\pm2\times10^{-4}$)
39	7.1×10^{-3} ($\pm2\times10^{-4}$)	1.68×10^{-3} ($\pm9\times10^{-5}$)
47	8.8×10^{-3} ($\pm3\times10^{-4}$)	0.9×10^{-3} ($\pm6\times10^{-5}$)
56	9.2×10^{-3} ($\pm3\times10^{-4}$)	0.54×10^{-3} ($\pm4\times10^{-5}$)
105	8.4×10^{-3} ($\pm3\times10^{-4}$)	0.28×10^{-3} ($\pm2\times10^{-5}$)
116	8.1×10^{-3} ($\pm3\times10^{-4}$)	0.22×10^{-3} ($\pm2\times10^{-5}$)
129	8.5×10^{-3} ($\pm3\times10^{-4}$)	0.19×10^{-3} ($\pm4\times10^{-5}$)

2. Detail of Free Energy Calculation

2.1. System

The system contains 4071 water molecules, one metal ion (Er^{3+} or Nd^{3+}), one deprotonated HDEHP molecule ($DEHP^-$) placed not far from the metal ion, and two Cl^- ions for electrical neutrality positioned far from the two interacting species. The simulation box is a cubic box of 50 Å in each dimension. Periodic boundary conditions are applied in all directions.

2.2. Force field

For water, we used a version of the flexible simple point charge (SPC) model with intramolecular potentials previous described by Kuchitsu and Morino.[7-8] The $DEHP^-$ molecule are modeled using the OPLS-UA force field,[5] while the potential for Er^{3+} and Nd^{3+} are modeled using the parameters that reproduce the correct ion-oxygen distance.[9] Non-bonded interactions are described with the conventional 12-6 Lennard-Jones (L-J) and Coulombic pairwise interaction:

$$U_{ij} = 4\varepsilon\left[\left(\frac{\sigma}{r_{ij}}\right)^{12} - \left(\frac{\sigma}{r_{ij}}\right)^{6}\right] + \frac{q_i q_j e^2}{4\pi\varepsilon_0 r_{ij}} \quad (2)$$

where ε is the depth of the potential well, σ is the zero inter-atom potential energy location, and ε_0 is the dielectric constant.

2.3. Methods

The free energy of the $DEHP^-$ phosphoric acid headgroup as a function of distance to the metal ion is determined by the umbrella method.[10-11] To start, the distance between the metal ion and the phosphorus atom (d_{MP}) is restrained in a harmonic potential with a force constant of 50 kcal·mol^{-1}Å^{-2}. The center of the harmonic potential is initially set at 8 Å where the $DEHP^-$ head group is moving freely. As the center is moved towards the metal ion with a step size of 0.1 Å, a classical molecular dynamics (MD) simulation is performed at each step for 2 ns at constant temperature (T = 300 K) until the center of the potential reaches 3.5 Å. This distance is smaller than the metal-

phosphorus distance in the stable metal-DEHP$^-$ complex. There are 46 biased distributions of d_{MP} that are collected to calculate the unbiased distribution of d_{MP} with the umbrella method, which is then used to calculate the free energy

$$A(d_{MP}) = -k_B T \ln P_{ub}(d_{MP}) \quad (3)$$

where k_B is the Boltzmann constant, T is the temperature of the simulation, and $P_{ub}(d_{MP})$ is the unbiased distribution of the metal-phosphorus (MP) distance.

3. Detail of Molecular dynamics simulation of aggregates formed in the aqueous solution

Molecular dynamics (MD) simulation was performed with the program GROMACS, version 4.50[12] using the OPLS-AA force field.[13] The TIP3P model was employed to describe the water molecules.[14] An aqueous box of 250×250×250 Å^3 contained 60 DEHP$^-$, 20 Er^{3+}, and 500,000 H_2O. The simulation was started by minimizing the energies of the initial configuration using the steepest descent algorithm. After energy minimization, a 1 ns constant-NPT simulation (time step 1 fs) was performed to obtain a reasonable size of solution box. A 0.5 ns constant-NVT simulation (time step 1 fs) was then performed to pre-equilibrate the system. Finally, a 100 ns constant-NVT simulation was then carried out to obtain the equilibrium state. Periodic boundary conditions were employed for all x-y-z directions. The temperature was controlled at 298 K with a Langevin thermostat.[15] The pressure was kept at 1 atm using a Langevin barostat.[16] The particle mesh ewald (PME) summation technique was used to calculate the long range electrostatic interactions.[17] The non-bonded interactions were calculated based on the Lennard-Jones (LJ) pair potentials, which assume interaction occurs between two bodies. LJ pair potentials were evaluated within a cut-off of 1.2 nm. The cross-interaction parameters were obtained from the Lorentz-Berthelot rules.[18] Trajectory analysis was partly done with the use of VMD.[19]

References

1. Hu, Z. S.; Pan, Y.; Ma, W. W.; Fu, X., Purification of Organophosphorus Acid Extractants. *Solvent Extr Ion Exc* **1995,** *13* (5), 965-976.
2. Swami, K. R.; Kumaresan, R.; Nayak, P. K.; Venkatesan, K. A.; Antony, M. P., Effect of pK(a) on the extraction behavior of Am(III) in organo phosphorus acid and diglycolamide solvent system. *Radiochim Acta* **2018,** *106* (2), 107-118.
3. Lin, B. H.; Meron, M.; Gebhardt, J.; Graber, T.; Schlossman, M. L.; Viccaro, P. J., The liquid surface/interface spectrometer at ChemMatCARS synchrotron facility at the Advanced Photon Source. *Physica B* **2003,** *336* (1-2), 75-80.
4. Sun, P.; Nowack, L. M.; Bu, W.; Bera, M. K.; Griesemer, S.; Reik, M.; Portner, J.; Rice, S. A.; Schlossman, M. L.; Lin, B. H., Free Thiols Regulate the Interactions and Self-Assembly of Thiol-Passivated Metal Nanoparticles. *Nano Lett* **2021,** *21* (4), 1613-1619.
5. Bu, W.; Mihaylov, M.; Amoanu, D.; Lin, B. H.; Meron, M.; Kuzmenko, I.; Soderholm, L.; Schlossman, M. L., X-ray Studies of Interfacial Strontium-Extractant Complexes in a Model Solvent Extraction System. *J Phys Chem B* **2014,** *118* (43), 12486-12500.
6. Bu, W.; Yu, H.; Luo, G. M.; Bera, M. K.; Hou, B. Y.; Schuman, A. W.; Lin, B. H.; Meron, M.; Kuzmenko, I.; Antonio, M. R.; Soderholm, L.; Schlossman, M. L., Observation of a Rare Earth Ion-Extractant Complex Arrested at the Oil Water Interface During Solvent Extraction. *J Phys Chem B* **2014,** *118* (36), 10662-10674.
7. Berendsen, H. J. C. P., J. P. M.; Gunsteren, W. F. V.; Hermans, J., *in Intermolecular Forces*. D. Reidel, Dordrecht: 1981.
8. Kuchitsu, K. M., Y., Estimation of Anharmonic Potential Constants. II. Bent XY2 Molecules. *Bull. Chem. Soc. Jpn* **1965,** *38*, 814.
9. Li, P. F.; Song, L. F.; Merz, K. M., Parameterization of Highly Charged Metal Ions Using the 12-6-4 LJ-Type Nonbonded Model in Explicit Water. *J Phys Chem B* **2015,** *119* (3), 883-895.

10. Roux, B., The Calculation of the Potential of Mean Force Using Computer-Simulations. *Comput Phys Commun* **1995,** *91* (1-3), 275-282.
11. Zhu, F. Q.; Hummer, G., Convergence and error estimation in free energy calculations using the weighted histogram analysis method. *J Comput Chem* **2012,** *33* (4), 453-465.
12. Hess, B.; Kutzner, C.; van der Spoel, D.; Lindahl, E., GROMACS 4: Algorithms for highly efficient, load-balanced, and scalable molecular simulation. *J Chem Theory Comput* **2008,** *4* (3), 435-447.
13. Damm, W.; Frontera, A.; TiradoRives, J.; Jorgensen, W. L., OPLS all-atom force field for carbohydrates. *J Comput Chem* **1997,** *18* (16), 1955-1970.
14. Jorgensen, W. L.; Chandrasekhar, J.; Madura, J. D.; Impey, R. W.; Klein, M. L., Comparison of Simple Potential Functions for Simulating Liquid Water. *J Chem Phys* **1983,** *79* (2), 926-935.
15. Feller, S. E.; Zhang, Y. H.; Pastor, R. W.; Brooks, B. R., Constant-Pressure Molecular-Dynamics Simulation - the Langevin Piston Method. *J Chem Phys* **1995,** *103* (11), 4613-4621.
16. Darden, T.; York, D.; Pedersen, L., Particle Mesh Ewald - an N.Log(N) Method for Ewald Sums in Large Systems. *J Chem Phys* **1993,** *98* (12), 10089-10092.
17. Cisneros, G. A.; Karttunen, M.; Ren, P. Y.; Sagui, C., Classical Electrostatics for Biomolecular Simulations. *Chemical Reviews* **2014,** *114* (1), 779-814.
18. Hirschfelder, J. O., Curtiss, C. F., Bird, R. B., *Molecular Theory of Gases and Liquids*. Wiley,: New York, 1964.
19. Humphrey, W.; Dalke, A.; Schulten, K., VMD: Visual molecular dynamics. *J Mol Graph Model* **1996,** *14* (1), 33-38.